KSUPT-98/2, KUNS-1505 May 1998

ARGO CMB Anisotropy Measurement Constraints on Open and Flat-Λ CDM Cosmogonies

Bharat Ratra[1], Ken Ganga[2], Radosław Stompor[3,4], Naoshi Sugiyama[5], Paolo de Bernardis[6], and Krzysztof M. Górski[7,8]

ABSTRACT

We use data from the **ARGO cosmic microwave background (CMB) anisotropy experiment** to constrain cosmogonies. We account for the ARGO beamwidth and calibration uncertainties, and marginalize over the offset removed from the data. Our derived amplitudes of the CMB anisotropy detected by the ARGO experiment are smaller than those derived previously.

We consider open and spatially-flat-Λ cold dark matter cosmogonies, with clustered-mass density parameter Ω_0 in the range 0.1–1, baryonic-mass density parameter Ω_B in the range $(0.005\text{–}0.029)h^{-2}$, and age of the universe t_0 in the range (10–20) Gyr. Marginalizing over all parameters but Ω_0, the ARGO data favors an open (spatially-flat-Λ) model with $\Omega_0 = 0.23$ (0.1), amongst the models considered.

At the 2 σ confidence level model normalizations deduced from the ARGO data are consistent with those drawn from the UCSB South Pole 1994, MAX 4+5, White Dish, and SuZIE data sets. The ARGO open model normalizations are also consistent with those deduced from the DMR data. However, for most spatially-flat-Λ models the DMR normalizations are more than 2 σ above the ARGO ones.

Subject headings: **cosmic microwave background**—cosmology: observations—**large-scale structure of the universe**

---

[1]Department of Physics, Kansas State University, Manhattan, KS 66506.

[2]IPAC, MS 100–22, California Institute of Technology, Pasadena, CA 91125.

[3]Institute of Astronomy, University of Cambridge, Madingley Road, Cambridge, CB3 0HA, UK.

[4]Copernicus Astronomical Center, Bartycka 18, 00-716 Warszawa, Poland.

[5]Department of Physics, Kyoto University, Kitashirakawa-Oiwakecho, Sakyo-ku, Kyoto 606-8502, Japan.

[6]Departimento di Fisica, Università di Roma La Sapienza, P. le A. Moro 2, I-00185 Roma, Italy.

[7]Theoretical Astrophysics Center, Juliane Maries Vej 30, 2100 Copenhagen Ø, Denmark.

[8]Warsaw University Observatory, Aleje Ujazdowskie 4, 00-478 Warszawa, Poland.

1. Introduction

Ganga et al. (1997a, hereafter GRGS) developed a general method to account for experimental and observational uncertainties, such as those in the beamwidth and the calibration, in likelihood analyses of cosmic microwave background (CMB) anisotropy data sets. In conjunction with theoretically-predicted CMB anisotropy spectra, this method has been used to account for beamwidth and calibration uncertainties in analyses of the Gundersen et al. (1995) UCSB South Pole 1994 data, the Church et al. (1997) SuZIE data, the MAX 4+5 data (Tanaka et al. 1996; Lim et al. 1996, and references therein), and the Tucker et al. (1993) White Dish data (GRGS; Ganga et al. 1997b, 1998; Ratra et al. 1998).

In this paper we present results from a similar analysis of the ARGO CMB anisotropy data set, but now consider a much larger range of cosmological-model parameter space. The 1993 flight of the balloon-borne ARGO experiment resulted in two data sets. One was from data taken in the direction of Hercules (de Bernardis et al. 1994a, hereafter deB94), and the second consisted of data taken in the direction of Aries and Taurus (Masi et al. 1996). In addition to the CMB signal, the Aries and Taurus data set is known to have a significant foreground dust signal in the shorter wavelength data with milder contamination in the longest wavelength data (Masi et al. 1995, 1996). To use the Aries and Taurus data to investigate CMB anisotropy one must carefully model this foreground dust contamination (Masi et al. 1996). In this paper we therefore only consider the deB94 Hercules data. De Bernardis et al. (1993) and Palumbo et al. (1994) describe the ARGO telescope and detectors. De Bernardis et al. (1994b) discuss the constraints that follow from the ARGO Hercules data on some cold dark matter (CDM) and other cosmological models.

ARGO data were taken in four wavelength bands centered at 0.5, 0.8, 1.2, and 2.0 mm (deB94). While there is dust contamination in the shorter wavelength data, the longest wavelength data is thought to be pure CMB anisotropy (deB94). Following deB94 we use only the 2 mm data for our CMB anisotropy analyses here.

The FWHM of the beam, assumed to be gaussian, is $52'$, with a 3% one standard deviation uncertainty. While observing, the beam was sinusoidally chopped with a half peak-to-peak chop amplitude of 0.9° on the sky. 63 points were observed with the payload performing azimuth step and integrate scans at constant elevation. This scan strategy, combined with sky rotation, produced a W-like scan pattern in equatorial coordinates (Figure 1 of deB94), sparsely sampling a region 1 hour wide in right ascension and 15° wide in declination. deB94 remove a single offset from the entire data set prior to binning. The ARGO Hercules scan absolute calibration uncertainty is 5% (one standard deviation)[9].

In §2 we summarize the computational techniques used in our analysis. See GRGS for a more detailed description. In §2 we also describe the greatly extended cosmological parameter space we

[9]The value quoted in deB94, 15%, is a higher standard deviation calibration uncertainty.

consider here. Results are given and discussed in §3. Conclusions are presented in §4.

2. Summary of Computation and Models Considered

The reduced 2 mm Hercules data is shown in Figure 1. The zero-lag window function for these observations is shown in Figure 2 and the zero-lag window function parameters are listed in Table 1.

Figure 2 also shows some of the model CMB anisotropy spectra used in the analysis. In earlier analyses (GRGS; Ganga et al. 1997b, 1998; Ratra et al. 1998), only a few (25) spectra were used. In this paper we use 798 spectra to cover a greatly extended range of the cosmological parameter space of the open and spatially-flat-Λ CDM models, and cover it with a higher resolution grid than previously used. This allows for an explicit construction of the full likelihood function as a function of all the cosmological parameters considered, and for making the various likelihood functions derived by marginalizing over parameters. This had not previously been possible.

We focus here on a spatially open CDM model and a spatially flat CDM model with a cosmological constant Λ. These low density models are consistent with most current observational constraints. For discussions see Coles et al. (1998), Bartelmann et al. (1998), Jenkins et al. (1998), Park et al. (1998), Merchán et al. (1998), Cole et al. (1998), Cavaliere, Menci, & Tozzi (1998), and Sommerville & Primack (1998).

The models have gaussian, adiabatic primordial energy-density power spectra. The flat-Λ model CMB anisotropy computations use a scale-invariant energy-density perturbation power spectrum (Harrison 1970; Peebles & Yu 1970; Zel'dovich 1972), as predicted in the simplest spatially-flat inflation models (Guth 1981; Kazanas 1980; Sato 1981a,b). The open model computations use the energy-density power spectrum (Ratra & Peebles 1994, 1995; Bucher, Goldhaber, & Turok 1995; Yamamoto, Sasaki, & Tanaka 1995) predicted in the simplest open-bubble inflation models (Gott 1982; Guth & Weinberg 1983). The computation of the CMB anisotropy spectra is described in Stompor (1994) and Sugiyama (1995).

The spectra are parameterized by their quadrupole-moment amplitude $Q_{\rm rms-PS}$, the clustered-mass density parameter Ω_0, the baryonic-mass density parameter Ω_B, and the age of the universe t_0. We have evaluated the spectra for a range of Ω_0 spanning the interval 0.1 to 1 in steps of 0.1, for a range of $\Omega_B h^2$ [the Hubble parameter $h = H_0/(100h \text{ km s}^{-1} \text{ Mpc}^{-1})$] spanning the interval 0.005 to 0.029 in steps of 0.004, and for a range of t_0 spanning the interval 10 to 20 Gyr in steps of 2 Gyr. Current observational estimates are more consistent with $\Omega_0 \sim 0.4$ (e.g., Cole et al. 1997; Eke et al. 1998), with $t_0 \sim 12$ Gyr (e.g., Reid 1997; Gratton et al. 1997), and disfavor $\Omega_B h^2$ larger than ~ 0.02 (e.g., Fukugita, Hogan, & Peebles 1998; Burles & Tytler 1998).

GRGS describe the computation of the likelihood function. Since deB94 remove an offset from the data, we assume a uniform prior in the amplitude of the offset removed and marginalize

over this amplitude when computing the likelihood function (Bond et al. 1991, Bunn et al. 1994; GRGS; Church et al. 1997; Ratra et al. 1998). This must be done since the removal of the offset also removes an undetermined amount of the CMB anisotropy signal from the data. Beamwidth and calibration uncertainties are accounted for as described in GRGS.

The open and flat-Λ model likelihoods are a function of four parameters: $Q_{\rm rms-PS}$, Ω_0, $\Omega_B h^2$, and t_0. We also compute marginalized likelihood functions by integrating over one or more of these parameters after assuming a uniform prior in the relevant parameters. The prior is set to zero outside the ranges considered for the parameters.

To derive central values and limits from the likelihood functions we assume a uniform prior in the relevant parameter, so the corresponding posterior probability density distribution function vanishes outside the chosen parameter range and is equal to the likelihood function inside this range. The deduced central value of the parameter is taken to be the value at which the posterior probability density peaks. The limits we quote are based on the highest posterior density (HPD) prescription. They are determined by integrating the posterior probability density starting at the peak and minimizing the difference between the upper and lower limits. The ± 1 σ and ± 2 σ HPD limits encompass 68.3% and 95.5% of the area, respectively. See GRGS for further details. Of course, the quoted limits depend on the prior range considered for the parameter, if the likelihood function is not sharply peaked within the range considered. This is the case for a number of the likelihood functions obtained below.

3. Results and Discussion

For the flat bandpower spectrum the ARGO likelihood peaks at bandtemperature $\delta T_l = 33$ μK, with a 1 σ range of 28 $\mu{\rm K} < \delta T_l < 38$ μK and likelihood ratio $= 1 \times 10^{21}$. For the fiducial CDM model spectrum $\delta T_l = 30$ μK, with 1 σ range 26 $\mu{\rm K} < \delta T_l < 35$ μK and likelihood ratio 5×10^{21}. These numerical values account for the marginalization over the offset removed from the data, as well as the beamwidth and calibration uncertainties. For fiducial CDM deB94 find that the likelihood peaks at $\delta T_l = 39$ μK, with 1 σ range 34 $\mu{\rm K} < \delta T_l < 45$ μK and likelihood ratio $= 5 \times 10^{23}$. The deB94 1 σ range accounts for calibration uncertainty by adding it in quadrature to the error bars derived ignoring it, but ignores offset removal and beamwidth uncertainty. The difference between the numerical values derived in deB94 and here is mostly because they have not marginalized over the amplitude of the offset removed while we have.

For the flat bandpower spectrum the ARGO average 1 σ δT_l error bar is $\sim 15\%$: ARGO data results in a very significant detection of CMB anisotropy, even after accounting for beamwidth and calibration uncertainties. For comparison, the corresponding DMR error bar is $\sim 10 - 12\%$ (depending on model, Górski et al. 1998). The MAX 4+5 data set also results in a small error bar $\sim 14\%$ (Ganga et al. 1998).

We note that δT_l values estimated using the flat bandpower and fiducial CDM spectra are

not identical. The variation in the deduced δT_l values from model to model is an indication of the accuracy of the flat bandpower approximation to the real spectrum over the range of the window function of the experiment. The variation from model to model found here is comparable to that found from the SP94 and MAX 4+5 data (GRGS; Ganga et al. 1998) but is smaller than that found from the SuZIE and White Dish data (Ganga et al. 1997b; Ratra et al. 1998).

For both the open and flat-Λ models, the four-dimensional posterior probability density distribution function $L(Q_{\rm rms-PS}, \Omega_0, \Omega_B h^2, t_0)$ is nicely peaked in the $Q_{\rm rms-PS}$ direction but quite flat in the other three directions. The dotted lines in Figure 3 illustrate this flatness in the (Ω_0, t_0) subspace of the flat-Λ model. Note that it is possible to distinguish between regions of parameter space at only slightly better than 0.25 σ confidence. The irregular solid lines in Figure 5 are the 2 σ contours of the four-dimensional posterior distribution projected on to the (Ω_0, $Q_{\rm rms-PS}$) subspace. They clearly show the steepness and peak (solid circles) in the $Q_{\rm rms-PS}$ direction.

Marginalizing over $Q_{\rm rms-PS}$ results in a three-dimensional posterior distribution $L(\Omega_0, \Omega_B h^2, t_0)$ which is steeper. The dashed lines in Figure 3 are the contours of this function. Note that it is now possible to distinguish between regions of parameter space at better than 1 σ confidence. Marginalizing over one more parameter (in addition to $Q_{\rm rms-PS}$) results in two-dimensional posterior probability distribution functions which are peaked (albeit, in most cases, at an edge of the parameter range considered, see the solid circle in Figure 3). It is now possible to distinguish between parts of parameter space at better than 3 σ confidence — see the solid lines in Figure 3.

As discussed below, caution must be exercised when interpreting the discriminative power of these formal limits, since they depend sensitively on the values of the parameters beyond which the uniform prior has been set to zero.

Figure 3 also illustrates a point noted earlier in the analysis of the MAX 4+5 data set (Ganga et al. 1998): conclusions about the most favored model drawn from the full four-dimensional posterior distribution tend to differ from those deduced from the three-dimensional posterior distribution derived by marginalizing the four-dimensional one over $Q_{\rm rms-PS}$. For example, from a similar plot of the (Ω_0, $\Omega_B h^2$) subspace of the open model (not shown), one finds that the four-dimensional distribution favors a large value of $\Omega_0 \sim 1$, while the three-dimensional distribution favors a small $\Omega_0 \sim 0.25$. As discussed in Ganga et al. (1998), this is a consequence of the asymmetry of the posterior distribution. This is not a significant issue since at the 2 σ confidence level the four-dimensional posterior distribution is flat in the Ω_0 direction and so it is not statistically meaningful to discuss how it varies with Ω_0.

As mentioned above, the two-dimensional posterior distributions (derived by marginalizing the four-dimensional distribution over two parameters at a time) allows one to distinguish between regions of parameter space at a higher level of confidence. Figure 4 illustrates this for the three cosmological parameters (Ω_0, $\Omega_B h^2$, t_0), for both the open and flat-Λ models. Certain parts of parameter space can now be formally ruled out at better than 2 σ significance. For example, for

the open model a region in parameter space centered near $\Omega_0 \sim 0.7$, $\Omega_B h^2 \sim 0.005$, and $t_0 \sim 10$ Gyr is ruled out at 3 σ. Again, caution must be exercised when interpreting the discriminative power of such formal limits.

Figure 5 shows the contours of the two-dimensional posterior distribution for $Q_{\rm rms-PS}$ and Ω_0, derived by marginalizing the four-dimensional distribution over $\Omega_B h^2$ and t_0. These are shown for the ARGO, DMR, SP94, MAX 4+5, White Dish, and SuZIE data sets, for both the open and flat-Λ models. For all but the DMR data we also show 2 σ confidence contours determined from projecting the four-dimensional posterior distribution on to this ($Q_{\rm rms-PS}$, Ω_0) subspace. Clearly, at 2 σ, constraints on these parameters derived from the ARGO data are mostly consistent with those derived from the other data sets. However, the DMR and ARGO data are more consistent for an open model than for the flat-Λ case, panels *a*) and *b*) of Figure 5. In fact, there is very little overlap between the 2 σ ranges (derived from the two-dimensional posterior distributions) of the ARGO and DMR normalizations for the flat-Λ models. There is, however, significant overlap between the 2 σ ranges derived by projecting the ARGO and DMR four-dimensional posterior distributions[10]. The SP94 results shown in panels *c*) and *d*) are those derived from the full Ka+Q data set. Sample variance and noise considerations indicate that the SP94 Ka band data is more consistent with what is expected for CMB anisotropy data (GRGS). At fixed Ω_0 the Ka band data results in a lower deduced $Q_{\rm rms-PS}$ (compared to that from the Ka+Q data, GRGS), so the SP94 Ka band results are more consistent with the ARGO results. The MAX 4+5 results shown in panels *e*) and *f*) of Figure 5 are those derived from the MAX 4 ID and SH and MAX 5 HR, MP, and PH data sets. Sample variance and noise considerations indicate that the MAX 4 ID and MAX 5 HR data are more consistent with what is expected for CMB anisotropy data (Ganga et al. 1998). This subset of the MAX 4+5 data has a lower $Q_{\rm rms-PS}$ (Ganga et al. 1998) and is thus more consistent with the ARGO data.

Figure 6 shows the one-dimensional posterior distribution functions for Ω_0, $\Omega_B h^2$, t_0, and $Q_{\rm rms-PS}$, derived by marginalizing the four-dimensional posterior distribution over the other three parameters. From these one-dimensional posterior distributions, ARGO data favors an open (flat-Λ) model with either $\Omega_0 = 0.23$ (0.10), or $\Omega_B h^2 = 0.029$ (0.020), or $t_0 = 20$ (12) Gyr, amongst the models considered. We emphasize that each of these are derived from one-dimensional posterior distributions and thus can not be simultaneously imposed. Also shown in Figure 6 are the limits derived from the one-dimensional distributions and the (projected) four-dimensional distribution. At 2 σ confidence the ARGO data only formally rules out small regions of parameter space. Specifically, from the one-dimensional posterior distributions, the ARGO data requires $\Omega_0 < 0.69$ or > 0.76 ($\Omega_0 < 0.91$), or $\Omega_B h^2 > 0.006$ ($\Omega_B h^2 > 0.006$), or $t_0 > 10$ Gyr ($t_0 < 20$ Gyr) for the open (flat-Λ) model at 2 σ. Since some of the one-dimensional posterior distributions

[10]Since the DMR four-dimensional posterior distribution is only very weakly dependent on $\Omega_B h^2$ and t_0, the confidence contours derived from this distribution projected on to the ($Q_{\rm rms-PS}$, Ω_0) plane are close to those derived from this distribution marginalized over $\Omega_B h^2$ and t_0.

peak at the edge of the parameter range considered some of these limits must be considered to be formal. Less controversially, it is clear that, for both open and flat-Λ models, ARGO data favors a low-density universe, although $\Omega_0 = 1$ is not strongly ruled out. Similarly, ARGO data also mildly favors a relatively large $\Omega_B h^2$ or a young (old) flat-Λ (open) model. As discussed above, ARGO results in fairly tight constraints on $Q_{\rm rms-PS}$ (panels g) and h) of Figure 6), and these are more consistent with the DMR results for the open model than for the flat-Λ case.

Care is needed when interpreting the discriminative power of such formal limits. Consider a posterior density function which is a gaussian and nicely peaked inside the parameter range considered. The 1 and 2 σ HPD limits for such a gaussian correspond to a value of the posterior distribution relative to that at the peak of 0.61 and 0.14 respectively. For the open model posterior distributions shown in Figure 6, the 1 and 2 σ HPD limits correspond to values of the posterior distribution relative to that at the peak of 0.63 & 0.56 (Ω_0), 0.95 & 0.91 ($\Omega_B h^2$), 0.93 & 0.86 (t_0), and 0.36 & 0.13 ($Q_{\rm rms-PS}$). It is hence probably fairer to conclude that the formal ARGO statistical limits on $\Omega_B h^2$ and t_0, and the 2 σ limits on Ω_0, should be taken much less seriously than those on $Q_{\rm rms-PS}$, and the 1 σ limits on Ω_0.

4. Conclusion

In our likelihood analyses of the ARGO Hercules scan CMB anisotropy data we have explicitly accounted for beamwidth and calibration uncertainties and have marginalized over the amplitude of the offset removed from the data. As a consequence the results derived here differ from those derived earlier. The ARGO results are mostly consistent with those derived from the DMR, SP94, MAX 4+5, White Dish and SuZIE data sets.

While the ARGO data does significantly constrain $Q_{\rm rms-PS}$ (and mildly constrain Ω_0), robust constraints on these and other cosmological parameters from the CMB anisotropy must await a models-based combined likelihood analysis of many different data sets.

We acknowledge helpful discussions with S. Masi, A. Noriega-Crespo, and G. Rocha. This work was partially carried out at the Infrared Processing and Analysis Center and the Jet Propulsion Laboratory of the California Institute of Technology, under a contract with the National Aeronautics and Space Administration. BR acknowledges support from NSF grant EPS-9550487 with matching support from the state of Kansas and from a K*STAR First award. RS acknowledges support from a UK PPARC grant and from Polish Scientific Committee (KBN) grant 2P03D00813.

Table 1: Numerical Values for the Zero-Lag Window Function Parameters[a]

$l_{e^{-0.5}}$	$l_{\rm e}$	$l_{\rm m}$	$l_{e^{-0.5}}$	$\sqrt{I(W_l)}$
60	97.6	109	168	0.551

[a]The value of l where W_l is largest, $l_{\rm m}$, the two values of l where $W_{l_{e^{-0.5}}} = e^{-0.5} W_{l_{\rm m}}$, $l_{e^{-0.5}}$, the effective multipole, $l_{\rm e} = I(lW_l)/I(W_l)$, and $I(W_l) = \sum_{l=2}^{\infty}(l+0.5)W_l/\{l(l+1)\}$.

REFERENCES

Bartelmann, M., Huss, A., Colberg, J.M., Jenkins, A., & Pearce, F.R. 1998, A&A, 330, 1

Bond, J.R., Efstathiou, G., Lubin, P.M., & Meinhold, P.R. 1991, Phys. Rev. Lett., 66, 2179

Bucher, M., Goldhaber, A.S., & Turok, N. 1995, Phys. Rev. D, 52, 3314

Bunn, E., White, M., Srednicki, M., & Scott, D. 1994, ApJ, 429, 1

Burles, S., & Tytler, D. 1998, ApJ, submitted

Cavaliere, A., Menci, N., & Tozzi, P. 1998, ApJ, in press

Church, S.E., Ganga, K.M., Ade, P.A.R., Holzapfel, W.L., Mauskopf, P.D., Wilbanks, T.M., & Lange, A.E. 1997, ApJ, 484, 523

Cole, S., Hatton, S., Weinberg, D.H., & Frenk, C.S. 1998, MNRAS, submitted

Cole, S., Weinberg, D.H., Frenk, C.S., & Ratra, B. 1997, MNRAS, 289, 37

Coles, P., Pearson, R.C., Borgani, S., Plionis, M., & Moscardini, L. 1998, MNRAS, 294, 245

de Bernardis, P., et al. 1993, A&A, 271, 683

de Bernardis, P., et al. 1994a, ApJ, 422, L33 (deB94)

de Bernardis, P., de Gasperis, G., Masi, S., & Vittorio, N. 1994b, ApJ, 433, L1

Eke, V.R., Cole, S., Frenk, C.S., & Henry, J.P. 1998, MNRAS, in press

Fukugita, M., Hogan, C.J., & Peebles, P.J.E. 1998, ApJ, in press

Ganga, K., Ratra, B., Gundersen, J.O., & Sugiyama, N. 1997a, ApJ, 484, 7 (GRGS)

Ganga, K., Ratra, B., Church, S.E., Sugiyama, N., Ade, P.A.R., Holzapfel, W.L., Mauskopf, P.D., & Lange, A.E. 1997b, ApJ, 484, 517

Ganga, K., Ratra, B., Lim, M.A., Sugiyama, N., & Tanaka, S.T. 1998, ApJS, 114, 165

Górski, K.M., Ratra, B., Stompor, R., Sugiyama, N., & Banday, A.J. 1998, ApJS, 114, 1

Gott, J.R. 1982, Nature, 295, 304

Gratton, R.G., Fusi Pecci, F., Carretta, E., Clementini, G., Corsi, C.E., & Lattanzi, M. 1997, ApJ, 491, 749

Gundersen, J.O., et al. 1995, ApJ, 443, L57

Guth, A. 1981, Phys. Rev. D, 23, 347

Guth, A.H., & Weinberg, E.J. 1983, Nucl. Phys. B, 212, 321

Harrison, E.R. 1970, Phys. Rev. D, 1, 2726

Jenkins, A., et al. 1998, ApJ, 499, 20

Kazanas, D. 1980, ApJ, 241, L59

Lim, M.A., et al. 1996, ApJ, 469, L69

Masi, S., et al. 1995, ApJ, 452, 253

Masi, S., de Bernardis, P., De Petris, M., Gervasi, M., Boscaleri, A., Aquilini, E., Martinis, L., & Scaramuzzi, F. 1996, ApJ, 463, L47

Merchán, M.E., Abadi, M.G., Lambas, D.G., & Valotto, C. 1998, ApJ, 497, 32

Palumbo, P., Aquilini, E., Cardoni, P., de Bernardis, P., De Ninno, A., Martinis, L., Masi, S., & Scaramuzzi, F. 1994, Cryogenics, 34, 1001

Park, C., Colley, W.N., Gott, J.R., Ratra, B., Spergel, D.N., & Sugiyama, N. 1998, ApJ, in press

Peebles, P.J.E., & Yu, J.T. 1970, ApJ, 162, 815

Ratra, B., Ganga, K., Sugiyama, N., Tucker, G.S., Griffin, G.S., Nguyên, H.T., & Peterson, J.B. 1998, ApJ, 505, in press

Ratra, B., & Peebles, P.J.E. 1994, ApJ, 432, L5

Ratra, B., & Peebles, P.J.E. 1995, Phys. Rev. D, 52, 1837

Ratra, B., Sugiyama, N., Banday, A.J., & Górski, K.M. 1997, ApJ, 481, 22

Reid, I.N. 1997, AJ, 114, 161

Sato, K. 1981a, Phys. Lett. B, 99, 66

Sato, K. 1981b, MNRAS, 195, 467

Sommerville, R.S., & Primack, J.R. 1998, MNRAS, submitted

Stompor, R. 1994, A&A, 287, 693

Stompor, R. 1997, in Microwave Background Anisotropies, ed. F.R. Bouchet, R. Gispert, B. Guiderdoni, & J. Tran Thanh Van (Gif-sur-Yvette: Editions Frontieres), 91

Sugiyama, N. 1995, ApJS, 100, 281

Tanaka, S.T., et al. 1996, ApJ, 468, L81

Tucker, G.S., Griffin, G.S., Nguyên, H.T., & Peterson, J.B. 1993, ApJ, 419, L45

Yamamoto, K., Sasaki, M., & Tanaka, T. 1995, ApJ, 455, 412

Zel'dovich, Ya.B. 1972, MNRAS, 160, 1P

This preprint was prepared with the AAS LaTeX macros v4.0.

Figure Captions

Fig. 1.— Measured 2 mm thermodynamic temperature differences (with ± 1-σ error bars) on the sky as a function of scan position in the direction of Hercules. Note that the 63 points in the scan are at varying right ascension and declination.

Fig. 2.— CMB anisotropy multipole moments $l(l+1)C_l/(2\pi) \times 10^{10}$ (solid lines, scale on left axis, note that these are fractional anisotropy moments and thus dimensionless) as a function of multipole l, for selected models normalized to the DMR maps (Górski et al. 1998; Stompor 1997). Panels $a) - c)$ show selected flat-Λ models. The heavy lines are the $\Omega_0 = 0.1$, $\Omega_B h^2 = 0.021$, and $t_0 = 12$ Gyr case, which is close to where the likelihoods (marginalized over all but one parameter at a time) are at a maximum. Panel $a)$ shows five $\Omega_B h^2 = 0.021$, $t_0 = 12$ Gyr models with $\Omega_0 =$ 0.1, 0.3, 0.5, 0.7, and 0.9 in descending order at the $l \sim 200$ peaks. Panel $b)$ shows seven $\Omega_0 = 0.1$, $t_0 = 12$ Gyr models with $\Omega_B h^2 = 0.029$, 0.025, 0.021, 0.017, 0.013, 0.009, and 0.005 in descending order at the $l \sim 200$ peaks. Panel $c)$ shows six $\Omega_0 = 0.1$, $\Omega_B h^2 = 0.021$ models with $t_0 = 20$, 18, 16, 14, 12, and 10 Gyr in descending order at the $l \sim 200$ peaks. Panels $d) - f)$ show selected open models. The heavy lines are the $\Omega_0 = 0.2$, $\Omega_B h^2 = 0.029$, and $t_0 = 20$ Gyr case, which is close to where the likelihoods (marginalized over all but one parameter at a time) are at a maximum. Panel $d)$ shows five $\Omega_B h^2 = 0.029$, $t_0 = 20$ Gyr models with $\Omega_0 = 1$, 0.8, 0.6, 0.4, and 0.2 from left to right at the peaks (the peak of the $\Omega_0 = 0.2$ model is off scale). Panel $e)$ shows seven $\Omega_0 = 0.2$, $t_0 =$ 20 Gyr models with $\Omega_B h^2 = 0.029$, 0.025, 0.021, 0.017, 0.013, 0.009, and 0.005 in descending order at $l \sim 600$. Panel $f)$ shows six $\Omega_0 = 0.2$, $\Omega_B h^2 = 0.029$ models with $t_0 = 20$, 18, 16, 14, 12, and 10 Gyr in descending order at $l \sim 600$. Also shown is the ARGO 2 mm zero-lag window function W_l (dotted lines, scale on right axis). See Table 1 for W_l-parameter values. The ARGO data mainly constrains the area under the product of the model spectrum and the window function on this plot. This is clearly larger for the DMR-normalized flat-Λ models than for the DMR-normalized open models. ARGO thus favors a lower relative normalization between the flat-Λ and open model than does the DMR.

Fig. 3.— Maxima and confidence contours of various posterior probability density distribution functions for the (Ω_0, t_0) subspace of the flat-Λ model. Dotted lines (solid squares) show the contours (maxima) of the four-dimensional $(Q_{\rm rms-PS}, \Omega_0, \Omega_B h^2, t_0)$ posterior distribution; contours of 0.1 and 0.25 σ confidence are shown. Dashed lines (solid triangles) show the contours (maxima) of the three-dimensional $(\Omega_0, \Omega_B h^2, t_0)$ posterior distribution (derived by marginalizing the four-dimensional one over $Q_{\rm rms-PS}$). Contours of 0.1, 0.25, 0.5, and 1 σ confidence are shown. Solid lines (solid circles) show the contours (maxima) of the two-dimensional posterior distribution (derived by marginalizing the four-dimensional one over the other two parameters). Contours of 1, 2, and 3 σ confidence are shown (the 3 σ contour is not labelled).

Fig. 4.— Confidence contours and maxima of the two-dimensional posterior probability density distribution functions, as a function of the two parameters on the axes of each panel (derived by marginalizing the four-dimensional posterior distribution over the other two parameters). Dashed lines (open circles) show the contours (maxima) of the open case and solid lines (solid circles) show those of the flat-Λ model. Contours of 0.25, 0.5, 1, 2, and 3 σ confidence are shown (3 σ contours are not labelled).

Fig. 5.— Confidence contours and maxima of the two-dimensional $(Q_{\rm rms-PS}, \Omega_0)$ posterior probability density distribution function. Panels *a*), *c*), *e*), and *g*) are for the flat-Λ model and panels *b*), *d*), *f*), and *h*) are for the open model. Note the different scale on the vertical $(Q_{\rm rms-PS})$ axis in each pair of panels. Shaded regions show the ARGO results, with denser shading for the 1 σ confidence region and less-dense shading for the 2 σ region. Irregular solid lines show the 2 σ confidence contours derived by projecting the four-dimensional ARGO posterior distribution in to this plane. [I.e., for each set of values of $(Q_{\rm rms-PS}, \Omega_0)$ we check if there is any choice of $\Omega_B h^2$ and t_0 such that the point $(Q_{\rm rms-PS}, \Omega_0, \Omega_B h^2, t_0)$ is within the 2 σ region of the four-dimensional ARGO posterior distribution. The projected 2 σ limits enclose those values of $(Q_{\rm rms-PS}, \Omega_0)$ for which such a point exists.] In panels *a*) $-$ *f*) hatched areas show the two-dimensional posterior probability density distribution function confidence regions for the DMR data (panels *a*) and *b*), Górski et al. 1998; Stompor 1997), the SP94 Ka+Q data (panels *c*) and *d*), GRGS), and the MAX 4+5 data (panels *e*) and *f*), Ganga et al. 1998). Heavy dashed confidence contours bounding these regions are labelled (except for the DMR cases); denser hatching corresponds to the 1 σ confidence region and less-dense hatching to the 2 σ confidence region. In panels *c*) $-$ *f*) unlabeled irregular light dashed lines show the 2 σ confidence contours derived by projecting the SP94 and MAX 4+5 four-dimensional posterior distributions in to this plane. Panels *g*) and *h*) show the SuZIE 2 σ upper limit (the hatched region bounded by the labelled heavy dashed line, Ganga et al. 1997b) and the White Dish 2 σ upper limit (labelled heavy dotted line in panel *h*) and not shown in panel *g*) since it is off scale, Ratra et al. 1998). The unlabeled irregular light dashed and dotted lines in panel *h*) are the corresponding SuZIE and White Dish 2 σ confidence upper limits derived by projecting the four-dimensional posterior distribution in to this plane (these limits are not shown in panel *g*) since they are off scale). Solid circles show the maxima of the ARGO two-dimensional posterior distribution and open circles show those of the other data sets (not shown for DMR, SuZIE, and White Dish). The DMR results are a composite of those from analyses of the two extreme data sets: i) galactic frame with quadrupole included and correcting for faint high-latitude galactic emission; and ii) ecliptic frame with quadrupole excluded and no other galactic emission correction (Górski et al. 1998).

Fig. 6.— One-dimensional posterior probability density distribution functions for Ω_0, $\Omega_B h^2$, t_0, and $Q_{\rm rms-PS}$ (derived by marginalizing the four-dimensional one over the other three parameters) in the open and flat-Λ models. Dotted vertical lines show the confidence limits derived from these one-dimensional posterior distributions and solid vertical lines in panels g) and h) show the ± 1 and ± 2 σ confidence limits derived by projecting the four-dimensional ARGO posterior distribution. The 2 σ DMR (marginalized and projected) confidence limits in panels g) and h) are a composite of those from the two extreme DMR data sets (see caption of Figure 5).

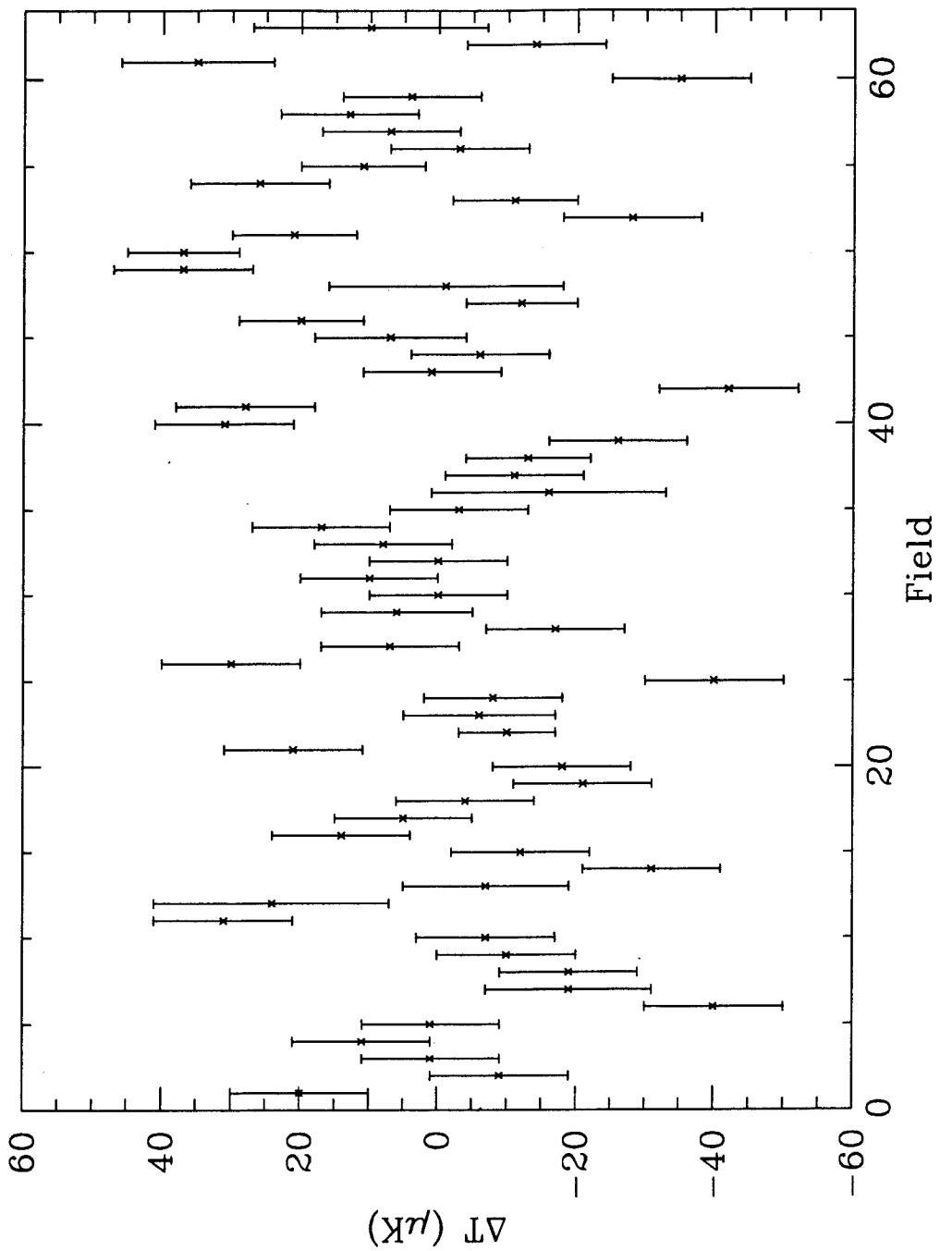

Figure 1

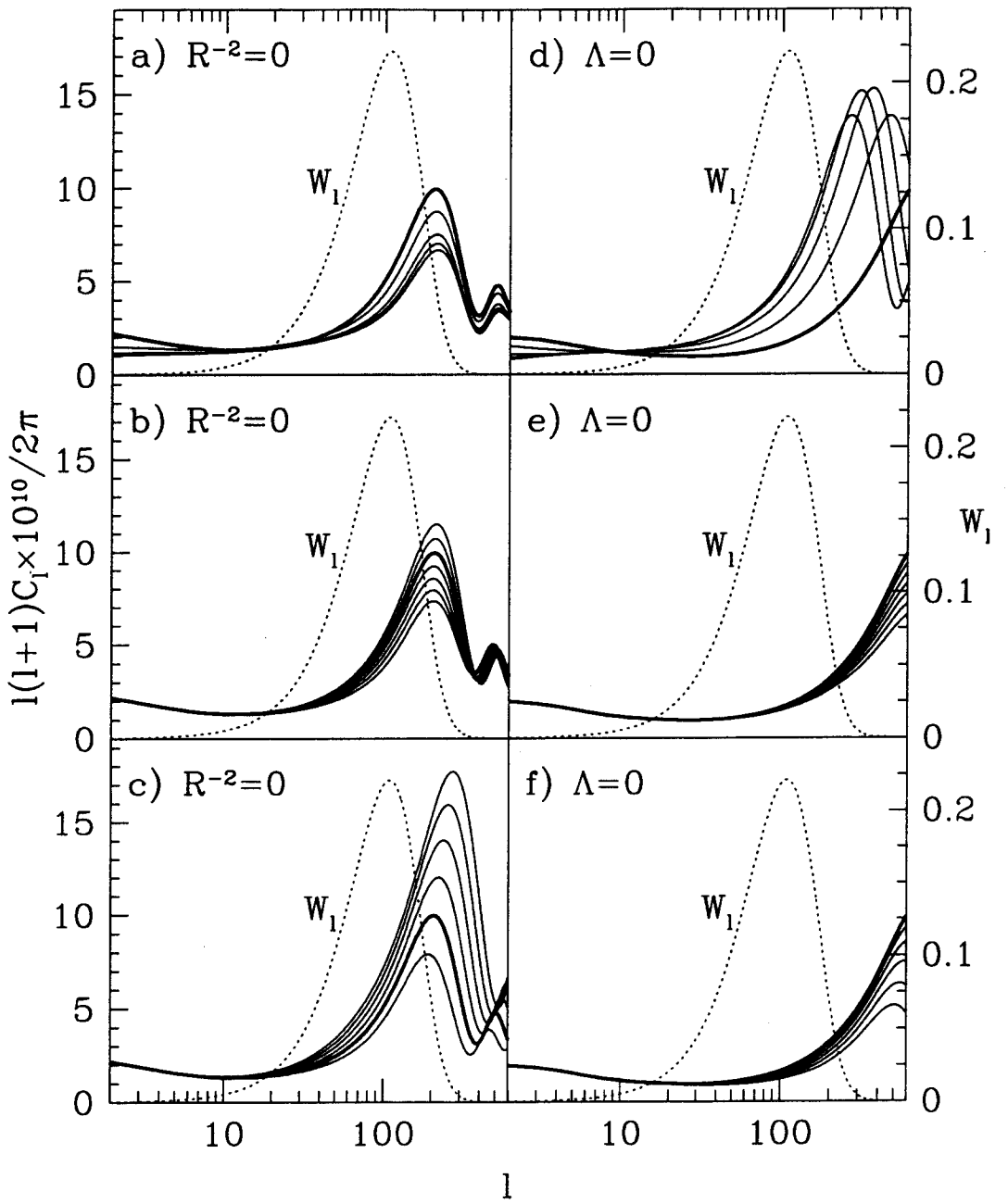
a) R⁻²=0
b) R⁻²=0
c) R⁻²=0
d) Λ=0
e) Λ=0
f) Λ=0
W_l
l(l+1)C_l×10¹⁰/2π
l
0
5
10
15
0.1
0.2
10
100

Figure 2

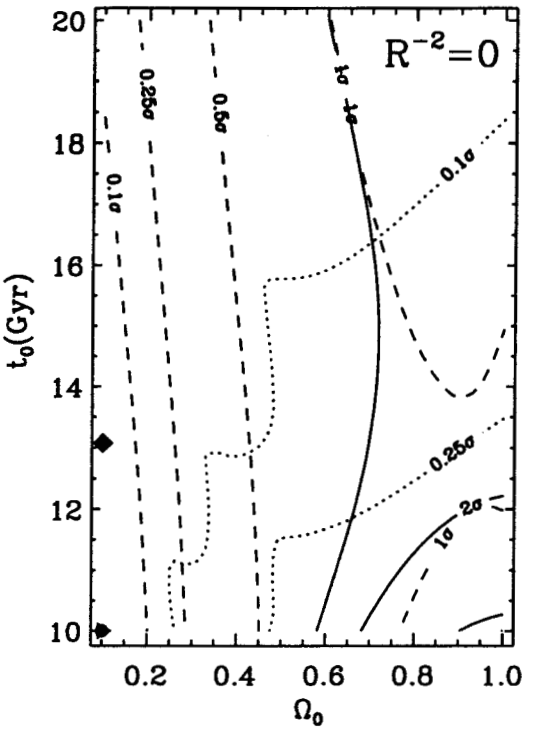
$R^{-2}=0$
0.1σ
0.25σ
0.5σ
1σ
0.1σ
0.25σ
1σ
2σ
20
18
16
14
12
10
0.2
0.4
0.6
0.8
1.0
t_0(Gyr)
Ω_0

Figure 3

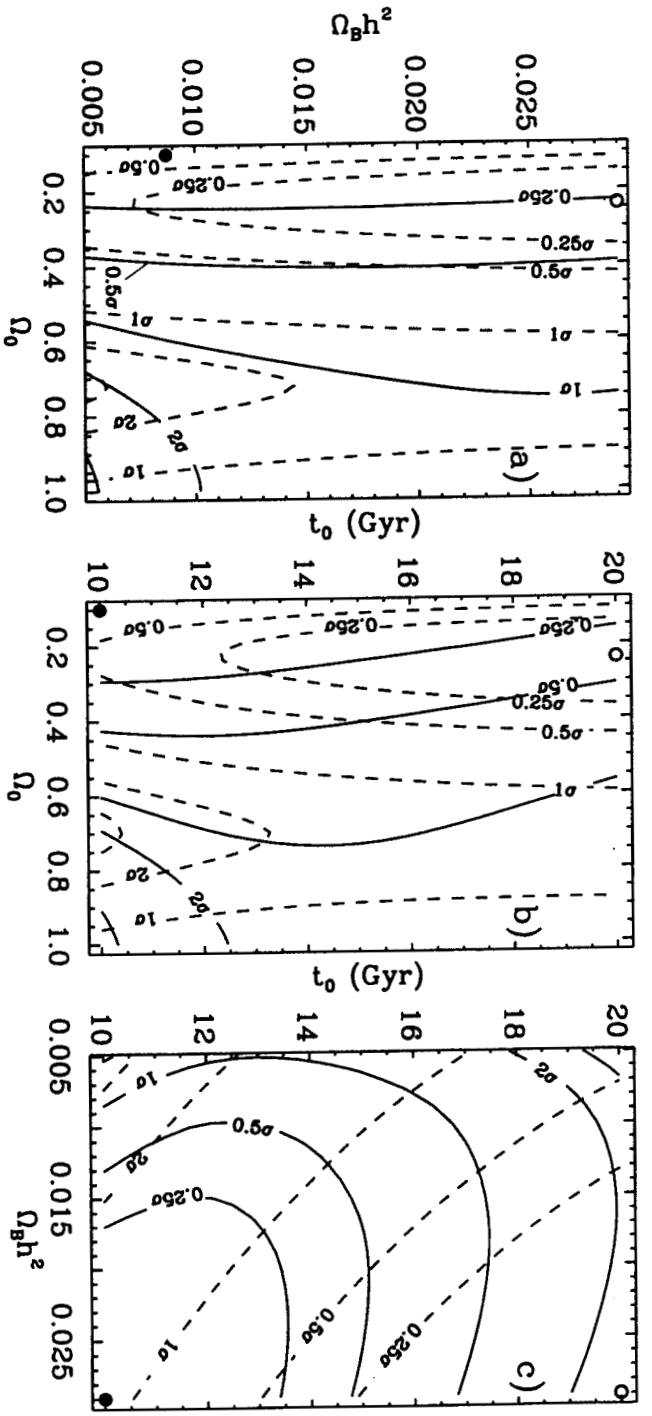
$\Omega_B h^2$
0.005
0.010
0.015
0.020
0.025
Ω_0
0.2
0.4
0.6
0.8
1.0
0.5σ
0.25σ
1σ
2σ
a)
t_0 (Gyr)
10
12
14
16
18
20
b)
c)

Figure 4

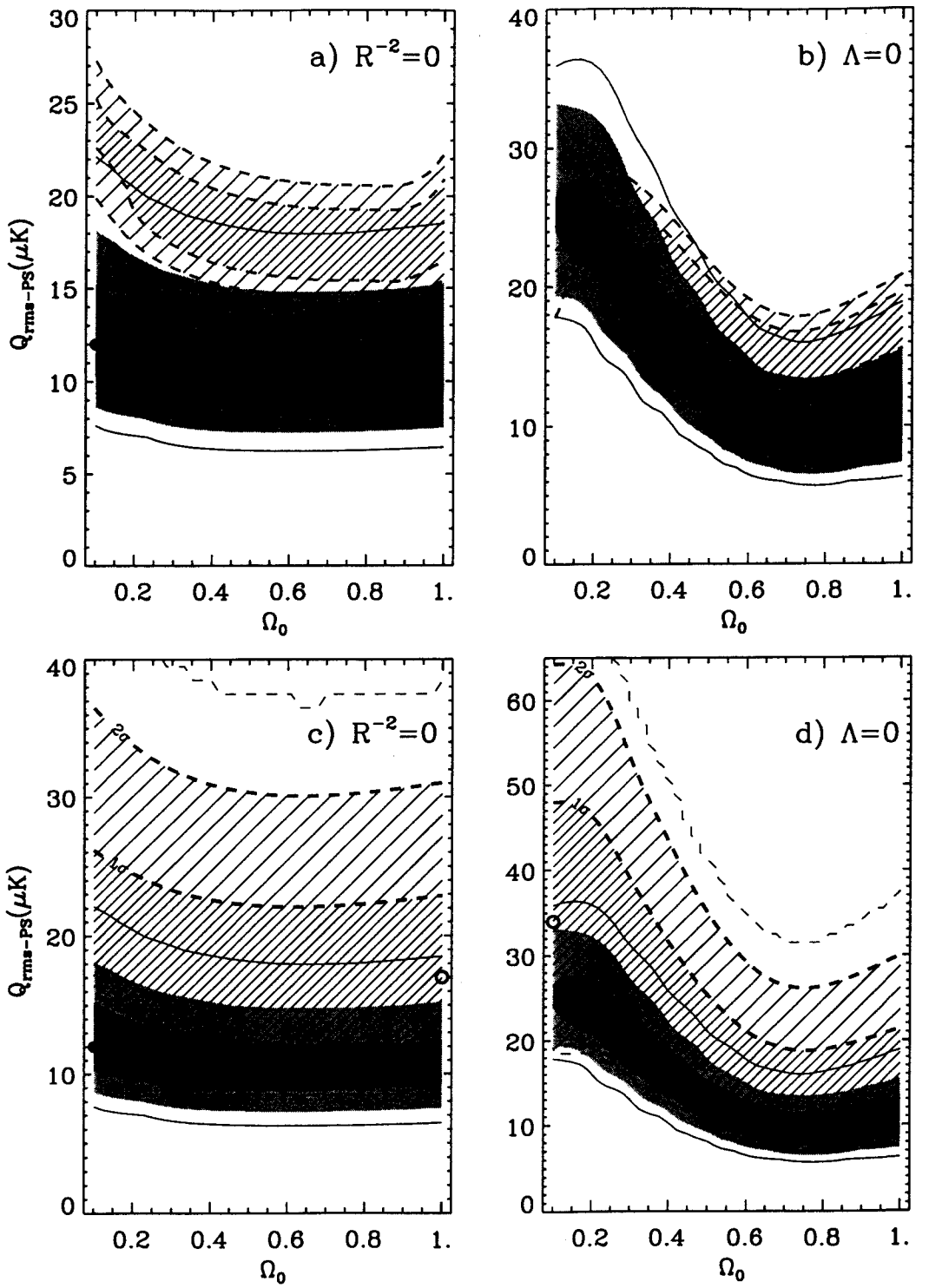

Figure 5.1

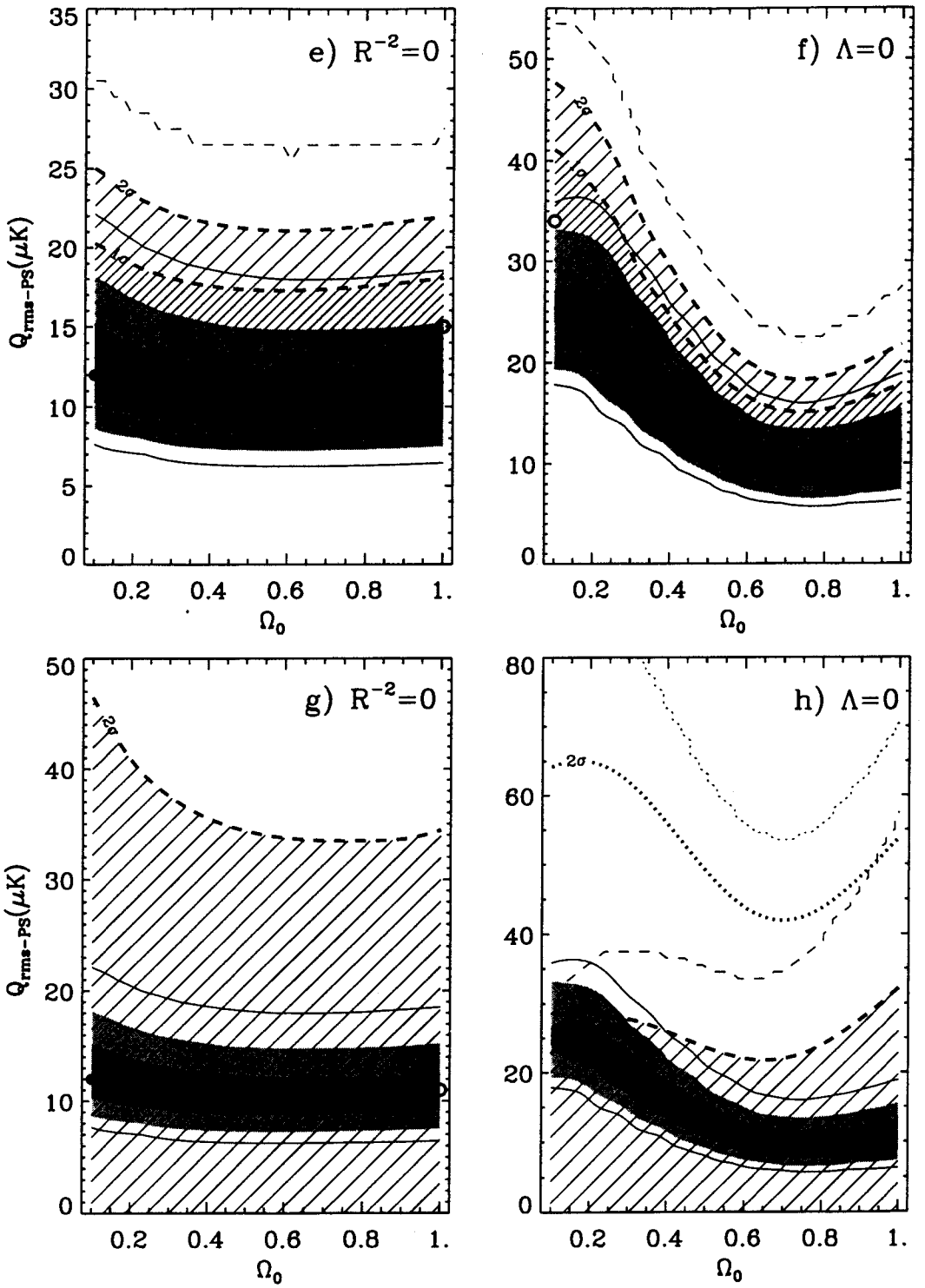

Figure 5.2

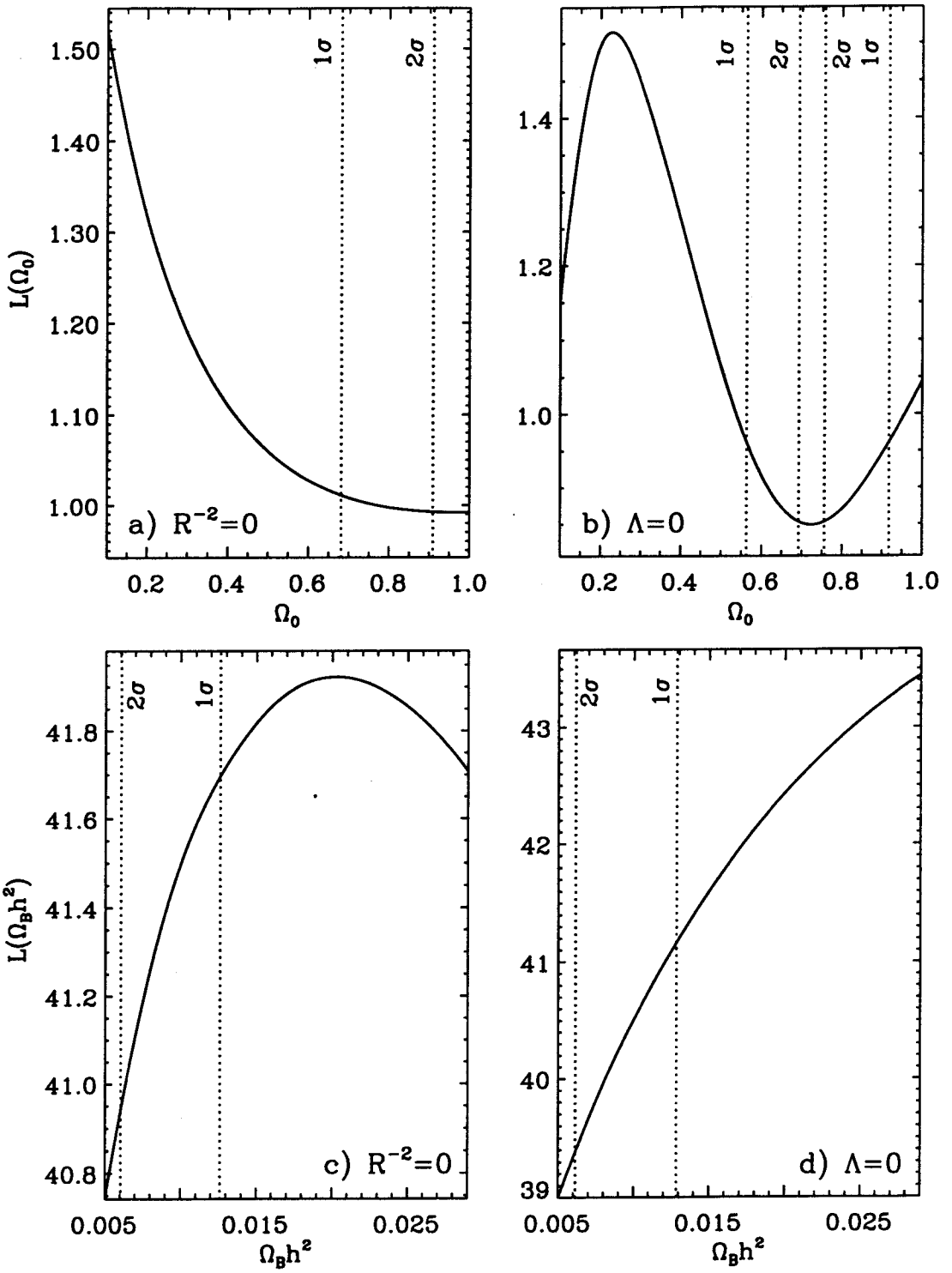
a) $R^{-2}=0$
b) $\Lambda=0$
c) $R^{-2}=0$
d) $\Lambda=0$
$L(\Omega_0)$
Ω_0
$L(\Omega_B h^2)$
$\Omega_B h^2$
1σ
2σ

Figure 6.1

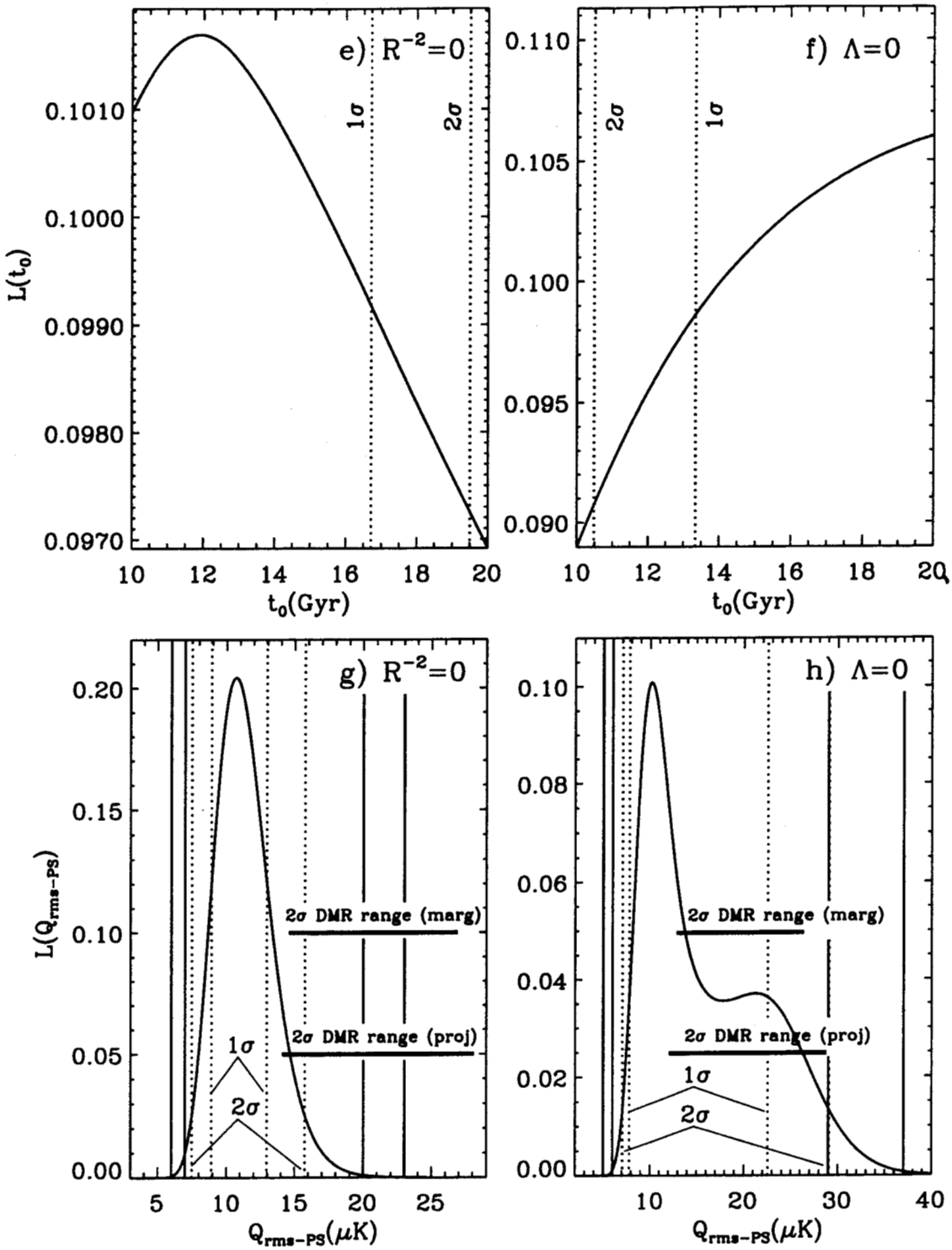
e) $R^{-2}=0$
f) $\Lambda=0$
1σ
2σ
$L(t_0)$
t_0(Gyr)
g) $R^{-2}=0$
h) $\Lambda=0$
2σ DMR range (marg)
2σ DMR range (proj)
$L(Q_{rms-PS})$
$Q_{rms-PS}(\mu K)$

Figure 6.2